JOURNAL OF GEOPHYSICAL RESEARCH, VOL. 103, NO. A4, PAGES 6827–6841, APRIL 1, 1998

Global configuration of the magnetotail current sheet as derived from Geotail, Wind, IMP 8 and ISEE 1/2 data

N. A. Tsyganenko,[1,6] S. B. P. Karlsson,[2] S. Kokubun,[3] T. Yamamoto,[4] A. J. Lazarus,[5] K. W. Ogilvie,[6] C. T. Russell,[7] and J. A. Slavin[6]

Abstract. Based on fine-resolution Geotail magnetometer data, a set of 5-min magnetic field averages was compiled for the period 1993–1997 and merged with 5-min average solar wind parameters, measured by IMP 8 and Wind spacecraft. Using this data set, the shape of the tail current sheet was studied in the interval $-100 < X_{GSM} < -10\,R_E$ as a function of the Earth's dipole tilt angle and of the B_y component of the IMF. The tilt-related warping of the current sheet and its twisting around the magnetotail axis in response to the IMF were modeled by analytical functions, whose parameters were found by least squares fitting to the data, for several bins of X_{GSM}. A similar modeling was also done for the near-tail region $-20 < X_{GSM} < -10\,R_E$, using a set of 5-min ISEE 1/2 data, tagged by corresponding solar wind parameters from IMP 8, for the entire duration of the ISEE magnetometer experiment (1977–1987). The IMF-related twisting steadily increases down the tail and is quite conspicuous even at close geocentric distances ($-20 \le X \le -10\,R_E$). A simple and flexible mathematical method is suggested, which allows quantitative modeling on a global scale of the IMF-related deformation of the cross-tail current by means of a "twist transformation" of the tail field. The method allows for a wide variety of possible geometries of the current sheet and keeps the total field confined within the magnetotail boundary. The results of the study are intended to be used in the development of an improved global model of the magnetospheric magnetic field, incorporating the effects of the IMF upon the magnetotail structure.

1. Introduction

The cross-tail current flowing in the magnetotail plasma sheet is a major source of the distant magnetospheric magnetic field. It is crucially important to have accurate quantitative information on its structure and dynamics in response to the varying orientation of the geodipole moment and to the changing state of the solar wind. The Earth's magnetotail has been extensively studied for more than three decades since its discovery in the early 1960s. It was realized early [e.g., *Russell and Brody*, 1967] that the diurnal and seasonal tilting of the Earth's dipole resulted in a significant periodic motion of the center of the tail current sheet perpendicular to the equatorial plane, while closer to the flanks the amplitude of the movement became smaller and even opposite to that near midnight. Since then, the effect was studied and revisited in numerous works, based on different data sets and techniques [e.g., *Bowling*, 1974; *Bowling and Russell*, 1976; *Fairfield*, 1980; *Gosling et al.*, 1986; *Dandouras*, 1988; *Nakai et al.*, 1997]. At the same time, the current sheet warping was incorporated in various quantitative models of the magnetosphere [e.g., *Voigt*, 1981; *Tsyganenko*, 1989, 1995, 1996; *Hilmer and Voigt*, 1995].

Another important factor, affecting the shape of the tail current sheet, is the transverse component of the interplanetary magnetic field. *Russell* [1972] was first to conjecture on the twisting action of the IMF B_y upon the tail, due to the asymmetry of the reconnection between the Earth's and the solar wind's magnetic fields. According to the theory, one should expect a left-handed twisting for IMF $B_y > 0$ and a right-handed one for IMF $B_y < 0$. *Cowley* [1981] addressed the twisting effect in the framework of simple quantitative models of the tail field, while *Sibeck et al.* [1985, 1986] provided first observational evidence, based on ISEE 3 data, of the effect in the deep tail. A quantitative study of distant tail twisting using finite Larmor radius effects, observed by the ISEE 3 energetic ion anisotropy spectrometer, was made by *Owen et al.* [1995]. Interestingly, this work showed larger tail twist for northward IMF B_z than for southward IMF B_z. *Tsyganenko* [1990] made a local modeling study of the IMF-

[1]Extraterrestrial Science Department, Hughes STX Corporation, Greenbelt, Maryland.

[2]Swedish Institute of Space Physics, Uppsala, Sweden.

[3]Solar-Terrestrial Environment Laboratory, Nagoya University, Japan.

[4]Institute of Space and Asronautical Science, Sagamihara, Japan.

[5]Massachusetts Institute of Technology, Center for Space Research, Cambridge.

[6]Laboratory for Extraterrestrial Physics, NASA Goddard Space Flight Center, Greenbelt, Maryland.

[7]Institute of Geophysics, University of California, Los Angeles.

Copyright 1998 by the American Geophysical Union.

Paper number 97JA03621.
0148-0227/98/97JA-03621$09.00

related twisting, using a set of magnetic field data from IMP spacecraft, tagged by hourly averages of the solar wind parameters. It was found that the current sheet twisting could be detected as close to Earth as $X \sim -30\,R_E$.

A longstanding limitation of the above studies was a very uneven coverage of the tail current sheet by the data. Almost 10 years of ISEE 1/2 magnetometer measurements (1977–1987) provided a good sampling in the near tail ($X_{GSM} \geq -23\,R_E$), making it possible to examine the transverse structure of the current sheet [*McComas et al.,* 1986], and yielded valuable information on the average configuration of the magnetotail in that region [e.g., *Nakai et al.,* 1997]. However, at larger distances the coverage remained relatively sparse. In spite of many years of IMP 8 observations in the tail at $-40 \leq X \leq -25\,R_E$, that spacecraft spent much of its time outside the plasma sheet, owing to a relatively high inclination and large radius of its nearly circular orbit. In addition, in many cases IMP 8 data were not supported by simultaneous monitoring of the solar wind state. At even larger distances the coverage of the tail was still worse: virtually no systematic measurements were made beyond $R \approx 40\,R_E$, except for a small set of Explorer 35 data in the vicinity of the lunar orbit and the data obtained from several passes of ISEE 3 in 1978–1982 [*Slavin et al.,* 1985].

This situation has been significantly improved since 1992, when the Geotail spacecraft was launched into orbit, specially designed for getting extensive coverage of the distant and near tail [*Kokubun et al.*, 1994; *Nishida,* 1994]. Owing to low inclination of its orbit, the spacecraft is spending much more time in the plasma sheet, making it possible to study in more detail the magnetotail plasmas and fields.

The present work takes advantage of the new opportunities offered by the Geotail magnetometer experiment and addresses the question of the shape of the cross-tail current as a function of the geodipole tilt angle and IMF B_y in the range of tailward distances $-100 \leq X \leq -10\,R_E$.

2. Data Selection

2.1. Solar Wind Data

The data on the solar wind ram pressure $P = \rho V^2$, its flow direction specified via velocity components V_x, V_y, V_z, and the interplanetary magnetic field were crucial both in the procedure of the selection of intramagnetospheric measurements, made by Geotail and ISEE 1/2, and in the modeling study itself. For that reason, we began the work from the preparation of the interplanetary medium data files.

We chose to use 5-min averaging intervals, for both the solar wind and the magnetospheric data. The reason behind that choice was that the characteristic solar wind travel distance for $\tau = 5$ min is of the order $\sim 20\,R_E$, roughly equal to the characteristic transverse scale size of the magnetosphere. It is therefore reasonable to assume 5 min as a lower limit for the characteristic response time of the magnetosphere to changes in the solar wind pressure. Assuming even smaller averaging intervals would result in unreasonably large data sets; on the other hand, using larger intervals could lead to a loss of information on the short-term variations of the magnetospheric field, induced by transient gusts of the solar wind.

Another important factor in selecting the interplanetary medium data is the location of the monitoring spacecraft with respect to the magnetosphere. Still in early studies of the consistency between ISEE 1 and ISEE 3 observations of the solar wind [*Crooker et al.*, 1982], it was found that the correlation became significantly worse for larger separation between the spacecraft, both along the Sun-Earth line and in the perpendicular direction. That finding was recently confirmed by *Slavin et al.* [1997] using data from Wind and IMP 8. For the most part of its operation period, Wind was located further upstream of the solar wind flow, with respect to IMP 8. For that reason, in this study preference was given to IMP 8 solar wind data [*King*, 1982], whenever they were available. However, IMP 8 spends roughly half of its time inside the magnetosheath and in the magnetosphere, and in addition to that, there are numerous tracking gaps, so that the total length of good-data intervals is even smaller, especially during the last years of the spacecraft's operation. Successful launch of Wind in the late 1994 provided a long-awaited opportunity to fill the gaps in the IMP 8 coverage [*Ogilvie et al.*, 1995; *Lepping et al.*, 1995].

In this study, the solar wind data were used for two purposes. First, information on the pressure and flow direction was used for determining the position of the model magnetopause, in order to select the data of Geotail taken inside the magnetosphere. Second, the selected magnetospheric data were tagged by simultaneous values of the solar wind parameters, in order to determine the response of the tail current sheet to solar wind conditions. In doing so, we took into account the time lag τ due to the separation between the solar wind (SW) monitor and the magnetospheric (MS) spacecraft. The lag was calculated by using the simple formula

$$\tau = (X_{SW} - X_{MS})/V_{SW} \tag{1}$$

where X_{SW} and X_{MS} are positions of the spacecraft along the Sun-Earth line and V_{SW} is the solar wind speed, measured at $X = X_{SW}$. This method implies that we only use a given 5-min tail field value if there exist time-shifted corresponding data on the solar wind plasma and IMF. It is also implicitly assumed in (1) that the magnetotail response to solar wind variations propagates downstream with approximately the same speed as the undisturbed solar wind outside the bow shock. This conjecture is strongly supported by a recent statistical analysis of the propagation of the solar wind disturbances down the tail, based on IMP 8 and Geotail data [*Kaymaz et al.,* 1995a], as well as by a case study of *Collier et al.* [1998].

Another inherent simplification of (1) is that it ignores possible effects of oblique disturbance boundaries in the solar wind, which can lead to significant errors in the calculated delay times, especially when the solar wind monitoring spacecraft is far from the Sun-Earth line [e.g., *Sergeev et al.*, 1986]. However, with only one spacecraft in the solar wind, there exist no simple operational method of taking that effect into account, so that using the simplest procedure based on (1) appears to be the only feasible choice.

Both IMP 8 and Wind data were processed in the same way. The first step was to reduce the original data files by averaging 1-min plasma data over 5-min intervals. The 5-min averages

of the IMF components were calculated by using 15-s data of IMP 8 or 1-min averages from the Wind magnetometer. Subsequently, the data were converted into GSM coordinates and merged with the solar wind plasma data files, so that each record in the output file contained simultaneous IMF and plasma information.

The next step was to filter the data by using an appropriate bow shock model, in order to eliminate possible measurements made inside the magnetosheath. We used the model of *Peredo et al.* [1995] with fixed parameters, having assumed the average solar wind pressure $\langle P_d \rangle = 3$ nPa and a relatively low Alfvenic Mach number $M_A = 4$. Using the average static model instead of a dynamical one should inevitably have resulted in a contamination of the solar wind data by magnetosheath measurements. However, since the bow shock size is relatively insensitive to the variations of the solar wind pressure, we do not expect the number of erroneous records to be significant.

Another source of data contamination can be related to erroneous values of the components of the solar wind velocity. As will be described below, we used the information on V_x, V_y, and V_z both in the selection of the magnetospheric data and for transforming them to the modified solar magnetospheric coordinate system, in which the X axis is parallel to the current direction of the solar wind. Visual inspection of the IMP 8 data revealed occasional large fluctuations of individual high-resolution values of the components of flow velocity against relatively stable or gradually varying background values. In most cases, such anomalous features were due to either an incorrectly analyzed mode of the plasma instrument or incorrect timing of Sun pulses. Unambiguous filtering out of the bad records was hardly possible, and therefore it was decided to reject all data with $|V_y|$ and $|V_z|$ larger than 30% and 20%, respectively, of the $|V_x|$, which resulted in a minor reduction of the data set.

2.2. Magnetospheric Data

2.2.1. Geotail data. In the compilation of the modeling database, we used 1-min vector averages of the magnetic field obtained during the period January 1, 1993 to July 20, 1997. The 1-min data were averaged over consecutive 5-min intervals, and then the data points were filtered by using a solar wind controlled magnetopause model. Each Geotail data point was first checked on whether a simultaneous (with an appropriate time lag) record with the solar wind plasma data existed. In the absence of such information, the data point was ignored; otherwise the point's location with respect to the magnetopause was checked. We used a pressure-driven model of the magnetopause, employed by *Tsyganenko* [1995, 1996] in the data-based magnetospheric field model. The magnetopause was represented by a composite surface, a prolate hemi-ellipsoid of revolution in the front (up to tailward distance of 50-70 R_E, depending on a pressure-dependent scaling factor), smoothly continued in the far tail by a cylinder of appropriate radius. The parameters of the ellipsoid corresponded to those found by *Sibeck et al.* [1991] for the average dynamical pressure of $\langle P_d \rangle = 2$ nPa, with the subsolar distance $R_S = 11\,R_E$, radius in the dawn-dusk meridian plane $R_D = 14.7\,R_E$, and the asymptotic tail radius $R_T = 28.4\,R_E$. The model magnetopause was assumed to self-similarly contract and expand in response to changes of the solar wind pressure, in accordance with the scaling factor $\kappa = \left(P_d/\langle P_d \rangle\right)^{\alpha}$, where the power index $\alpha = 0.14$ was specified as previously found from fitting the data-based model of the magnetospheric field to data [*Tsyganenko*, 1996].

The axis of symmetry of the model magnetopause was chosen to be parallel to the observed direction of the solar wind, specified by the vector $\{V_x, V_y, V_z\}$, rather than by the Sun-Earth line. In other words, the position of every Geotail data point with respect to the model magnetopause was defined in the "geocentric solar wind magnetospheric" (GSWM) coordinate system (described in more detail in the appendix), rather than in the standard GSM one. The data points located outside the model boundary and those with $X_{GSWM} < -100\,R_E$ were rejected.

Finally, the magnetospheric field data were tagged by the corresponding solar wind parameters and binned into seven intervals of the coordinate X_{GSWM}: $-15 \le X < -10\,R_E$, $-20 \le X < -15\,R_E$, $-25 \le X < -20\,R_E$, $-30 \le X < -25\,R_E$, $-40 \le X < -30\,R_E$, $-60 \le X < -40\,R_E$, and $-100 \le X < -60\,R_E$. The lengths of the intervals were chosen to increase tailward, in order to keep the number of data points in the individual bins sufficiently large and thus compensate for the decrease of the number of data points at larger distances. Also, the magnetotail becomes more uniform with increasing tailward distance, which justifies the increase of the length of the bins.

Besides the requirement that each magnetospheric data point be provided by corresponding values of the solar wind pressure, lagged for the solar wind travel time, the data were also tagged by the corresponding values of the IMF components. However, since the IMF effects are known to develop with an additional time delay, associated with the merging and magnetic flux transfer processes, we increased the time lag when tagging the data by the values of IMF components. Specifically, every magnetospheric data point was provided by a value of the IMF B_y, averaged over 15-min interval, whose center was shifted back in time by 30 min, in addition to the time lag due to the solar wind travel time. The question on the optimal way of taking into account the IMF effects is an important and interesting problem; however, it extends beyond the framework of the present work.

Figure 1 shows the distribution of the data points in projection on the tail cross sections in the geocentric solar ecliptical (GSE) coordinates, for each of the seven bins. In the first four bins corresponding to $X_{GSE} > -30\,R_E$, the data are distributed within narrow bands located close to the equatorial plane. The data coverage in three distant bins with $X < -30\,R_E$ is also quite nonuniform and localized within narrow intervals of the Z coordinate; here the points are further away from the equatorial plane, and their number is much less here than in the near tail.

Figure 2 displays the data points in the same format, but in the geocentric solar magnetospheric (GSM) coordinates, which are more appropriate for studying the magnetospheric structure. Owing to seasonal and diurnal wobbling of the geodipole and related rotation of the GSM Y and Z axes around the Sun-Earth line, the data distribution gains much spread about the GSM equatorial plane, especially near the plasma sheet flanks.

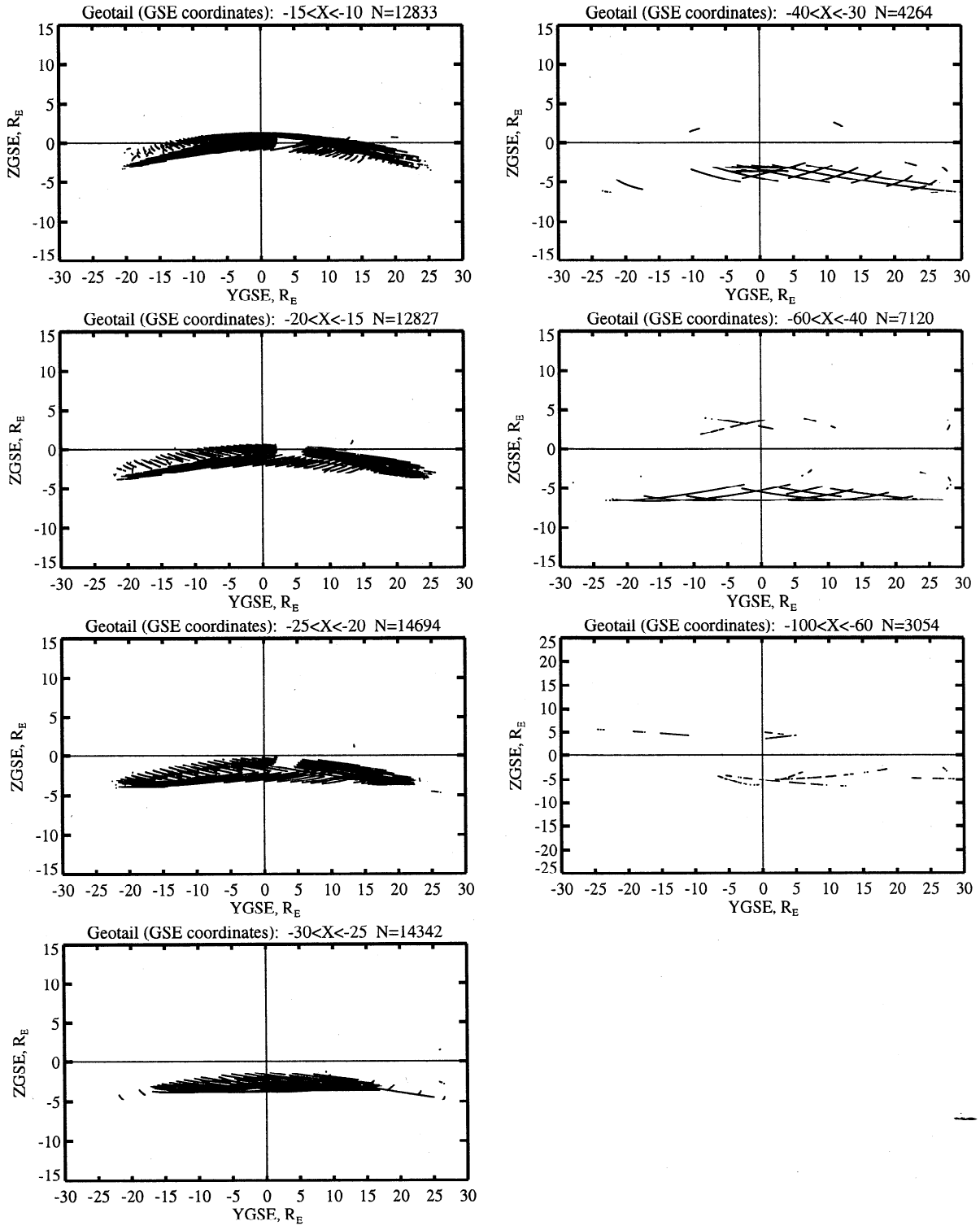

Figure 1. Coverage by Geotail data for the individual bins of tailward distance, displayed in geocentric solar ecliptic (GSE) coordinates.

Transformation of the data point coordinates from the GSM to the solar wind magnetospheric system, based on the actual direction of the flow, results in a further dramatic change of the spatial distribution of the data. Figure 3 shows the same data in the GSWM coordinates, and one can see that their pattern differs strikingly from that in the previous plots: instead of smoothly lining along the spacecraft orbit, as in Figures 1 and 2, the data points are strongly scattered over a wide area, owing to incessant large-amplitude fluctuations of the solar wind flow direction and the related windsock-like flapping of the magnetotail. When calculating the position of the GSWM coordinate axes for every individual data point, we took into account appropriate time lags due to the finite speed of the solar wind; however, it was also assumed that, on

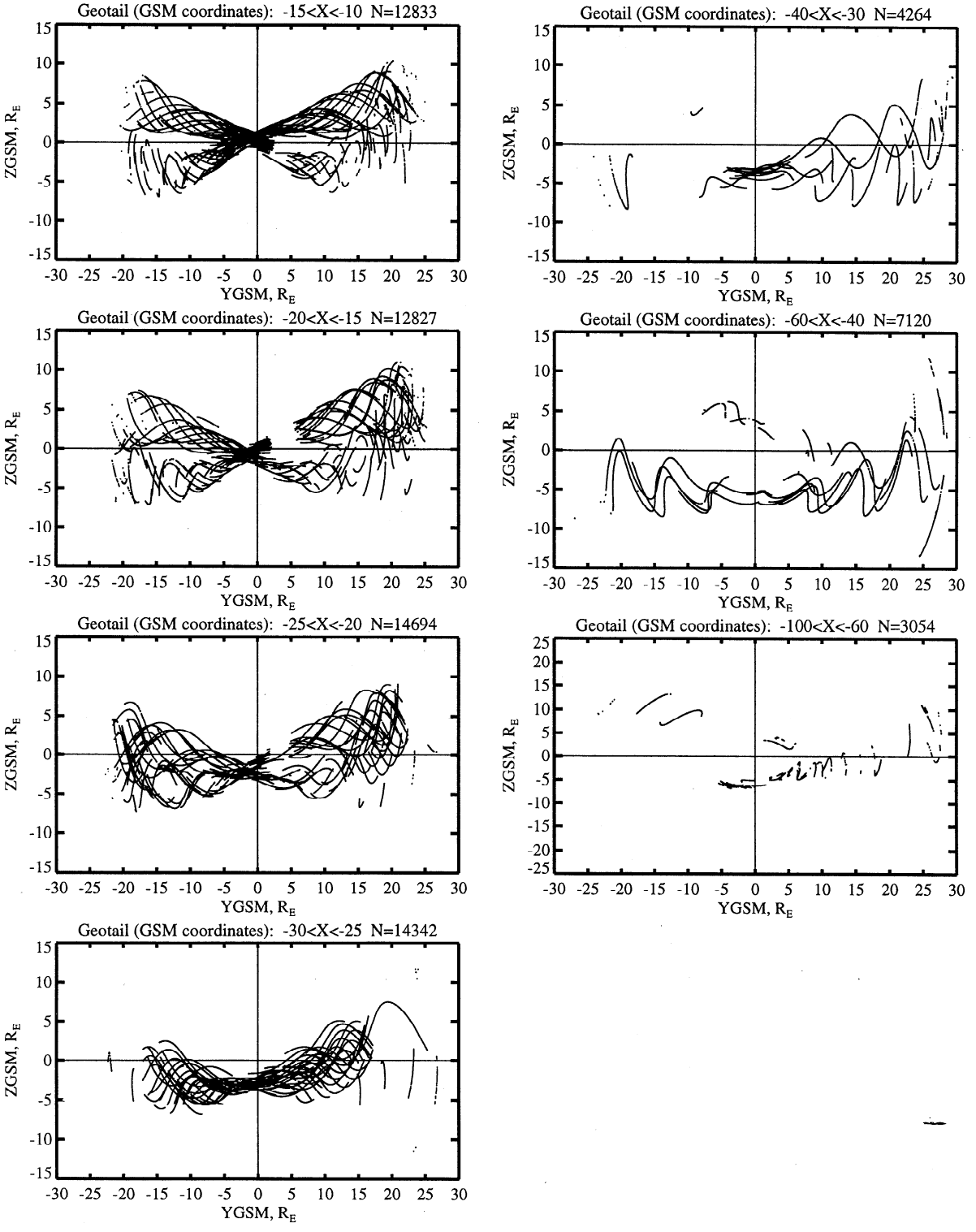

Figure 2. Same as in Figure 1, but in geocentric solar magnetospheric (GSM) coordinates. Note a larger spread of the data due to the wobbling of the Earth's dipole.

the 5-min time scale, the tail's response to the change in the flow angle was instantaneous. In other words, no additional lag was introduced to allow for a finite time of the tail rotation into a new position, corresponding to the new direction of the solar wind. Owing to a relatively high density of the solar wind flow in comparison with that of the tail plasma population, the windsock effect should be of a mainly kinematic nature, and hence the additional time lag is unlikely to be significant.

As can be seen in Figure 3, the large scatter of the data points in the GSWM coordinates widens the limits of the coverage of the equatorial region and makes it much more uniform, which should improve the chances for successfully determining the average shape of the current sheet at large

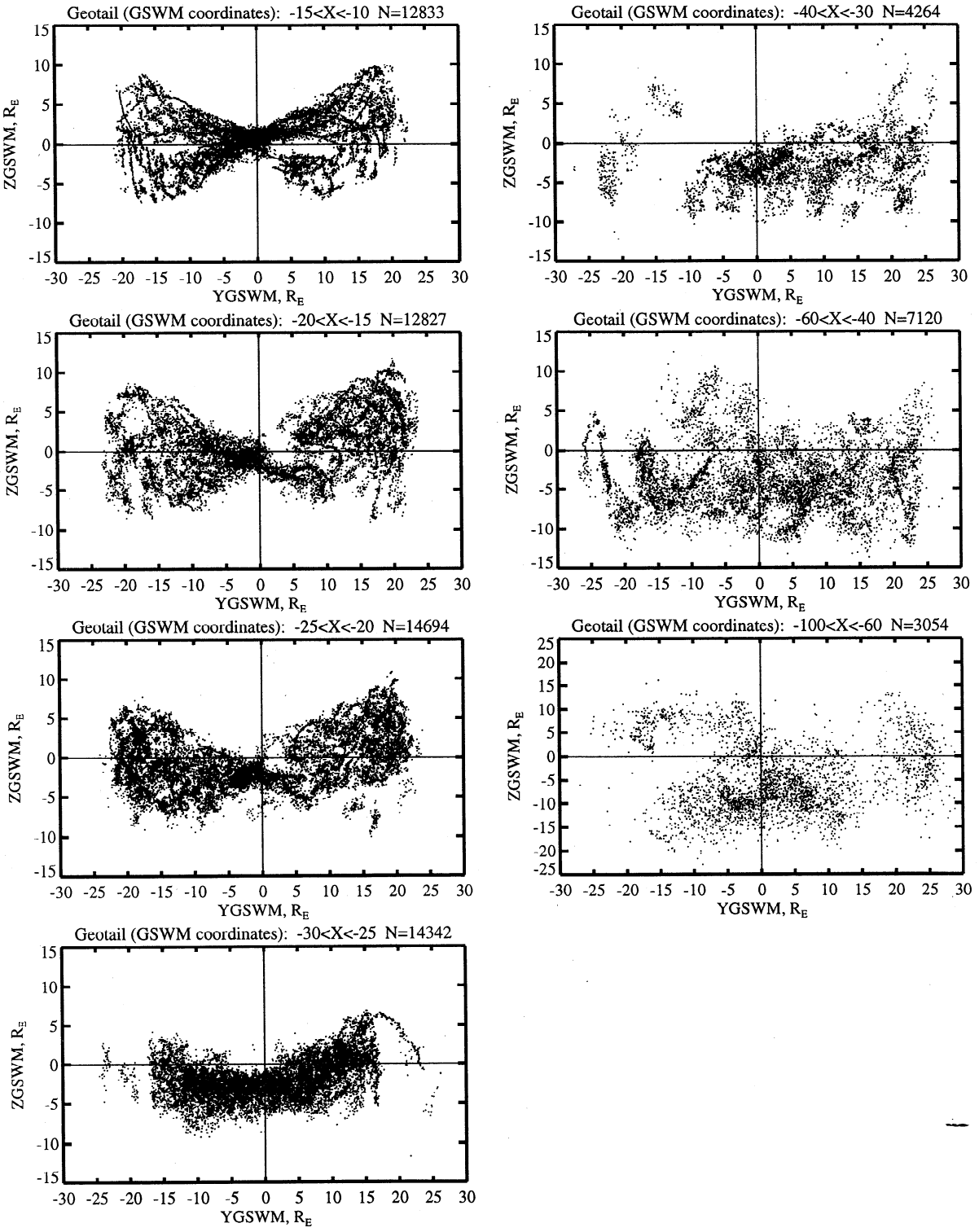

Figure 3. Same as in Figures 1–2, but in geocentric solar wind magnetospheric (GSWM) coordinates. Note a strong scatter of the data due to fluctuations in the solar wind direction.

distances. On the other hand, the variability of the flow direction of the solar wind, combined with inaccuracies of our simple procedure of taking into account the spacecraft separation, various fluctuations, and remaining instrumental effects in the determination of the flow angles, introduces its own errors in the calculation of Y_{GSWM} and Z_{GSWM}. These errors rapidly increase in magnitude as we move tailward and impose an upper limit on the applicability of the method in the distant tail. Nonetheless, as shown below, our procedure still provides quite reasonable results up to $\sim 100\ R_E$ down the tail.

It is also noteworthy that, as one can see in Figure 3, the data points in the bins with $X < -20\ R_E$ tend to concentrate southward from the GSWM equatorial plane. Fortunately,

this shift matches the average location of the cross-tail current for the corresponding time intervals and, hence, further improves the coverage of the most important region. Indeed, as can be seen from Table 1, the average values of the geodipole tilt angle for the bins in the interval $-60 \le X < -20\,R_E$ are between $-16°$ and $-20°$. Based on the average value of the "hinging distance" $R_H \sim 9\,R_E$ (equation (2) below), we therefore can expect the current sheet to be located, on the average, at $Z \sim -3\,R_E$, which falls roughly in the middle of the data distribution, as can be seen in Figure 3.

2.2.2. ISEE 1/2 data. The ISEE 1/2 data set was created by using 1-min averages from the National Space Science Data Center Summary Data tapes, covering the entire nearly 10-year period of the magnetometer experiment, from October 1977 to July 1987 [*Russell*, 1978]. The data were visually inspected, intervals of good data taken inside the magnetosphere were selected, and the data were averaged over 5-min intervals and tagged by the IMP 8 data, being properly lagged in time in order to take into account the finite speed of the solar wind. Because of the relatively low apogee of the ISEE spacecraft ($\approx 24\,R_E$), their data were binned into only two intervals of X, namely, $-15 \le X_{GSM} < -10\,R_E$ and $-20 \le X_{GSM} < -15\,R_E$, and the data were not transformed to the GSWM coordinate system.

As in the case of Geotail data, we also introduced additional time lag for the IMF data, but it was also required that every ISEE data record was tagged by 10 consecutive 5-min average values of the IMF components, with the goal to use those data in a future study of the optimal method for taking into account IMF effects. Owing to that requirement, the size of the final ISEE data set was significantly reduced; however, owing to the very long duration of the experiment, the numbers of the data records in the bins were still quite large, 8995 for the sunward bin and 8340 for the tailward one.

Figure 4 displays the distribution of the data points within the individual bins. Because of the large difference in the orbital parameters, the coverage by the ISEE data for the same X bins markedly differs from the similar plots for the Geotail data in Figures 2 and 3. Because of lower apogee, the coverage in the tailward bin is narrower in the Y direction than in the sunward one. At the same time, the data span a significantly larger interval of Z, which results in a somewhat poorer coverage of the equatorial region.

3. Modeling the Cross-tail Current Sheet

In this work, the global geometry of the cross-tail current sheet was studied by deriving a set of local models, using the magnetic field data for several bins of the X coordinate. In doing so, we did not attempt to construct representations for the full vector of the magnetic field, but used its B_x component only, since it is the most sensitive indicator of the position of the current sheet. Another simplifying assumption is the absence of variations in the X direction within individual bins, which is justified by the limited extensions of the bins along the Sun-Earth line.

We assume that B_x smoothly varies in the direction perpendicular to a warped neutral sheet, changing its sign on crossing that sheet and approaching asymptotic values $\pm B_0$ in the tail lobes. The characteristic scale of the B_x variation corresponds to the thickness of the current sheet and can be defined as a free parameter of the model. A simple example of this kind of model is the one-dimensional planar current sheet by *Harris* [1962], in which $B_x = B_0 \tanh(Z/Z_0)$.

In our case the problem is somewhat complicated by the fact that the current sheet is warped in the YZ plane. For that reason, in order to determine positions of the data points with respect to the current sheet, we need to define a pair of curvilinear coordinates $\{\eta, \zeta\}$ by introducing an appropriate transformation of the original coordinates $\{Y, Z\}$. First of all, however, we need to specify the shape of the warped current sheet.

We define a simple approximation for the position of the center of the current sheet as a function of the distance Y from the midnight meridian plane, of the dipole tilt angle Ψ, and of the IMF B_y:

$$Z_s(Y) = \left(R_H - G\frac{Y^4}{Y^4 + L_y^4}\right)\sin\Psi + \left(T_1\frac{Y}{L_y} + T_2\frac{Y^2}{L_y^2}\,\mathrm{sign}Y\right) B_y^{IMF} \qquad (2)$$

This simple model includes five parameters, the hinging distance R_H [e.g., *Russell and Brody*, 1967], the warping amplitude G, two coefficients T_1 and T_2 which parameterize the twisting effect, and the characteristic extension L_y of

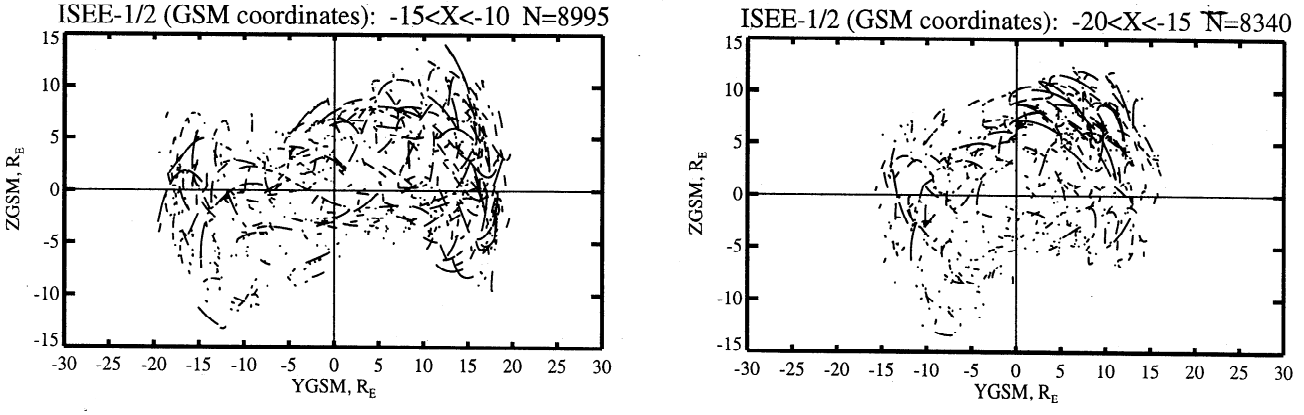

Figure 4. Coverage by ISEE 1/2 data for two near-tail bins, displayed in GSM coordinates (GSM). Note a significant difference from the Geotail coverage for the same bins (Figure 2).

the sheet deformation in the YZ plane. The first term on the right-hand side of (2) represents the dependence on the geodipole tilt and is similar to that employed by *Tsyganenko* [1989, 1995, 1996]. The second term is responsible for the twisting effect; it includes the purely rotational part with the coefficient T_1, in which the shift in Z direction is a linear function of Y, as well as the quadratic term, controlled by the coefficient T_2 and introduced in order to allow for possible variation of the twisting angle toward the magnetotail flanks. Such a complex twisting was found by *Kaymaz et al.* [1995b], based on IMP 8 measurements at $-40 < X < -25\ R_E$.

Having defined the shape of the reference current sheet (2), we can introduce curvilinear coordinates $\{\eta, \zeta\}$ as follows. Using the function $Z_s(Y)$ from (2), define $\Phi(Y, Z) = Z - Z_s(Y)$, so that the equality $\Phi = 0$ corresponds to the sheet, while the lines $\Phi(Y, Z) = C \neq 0$ form a family of contours of similar shape, lying at different distances from the latter. In the linear approximation, the transverse distance from a point (y, z) to the central sheet (2) equals

$$\zeta = \frac{\Phi(y, z)}{|\nabla\Phi(y, z)|} \tag{3}$$

and this is the second coordinate we need. Note, again, that its definition is essentially based on the Taylor expansion of the function $\Phi(y, z)$ around the central sheet; so it is not exactly equal to the actual distance from the latter, but provided the data points lie not too far from the sheet (more specifically, closer than its curvature radius), the accuracy is quite sufficient for our purposes.

In contrast to ζ, the choice of the first coordinate, η, is not critical for our study, because the field variation is much slower in the direction parallel to the current sheet than across it. In particular, we do not need to require that the two families of the coordinate lines be precisely orthogonal to each other.

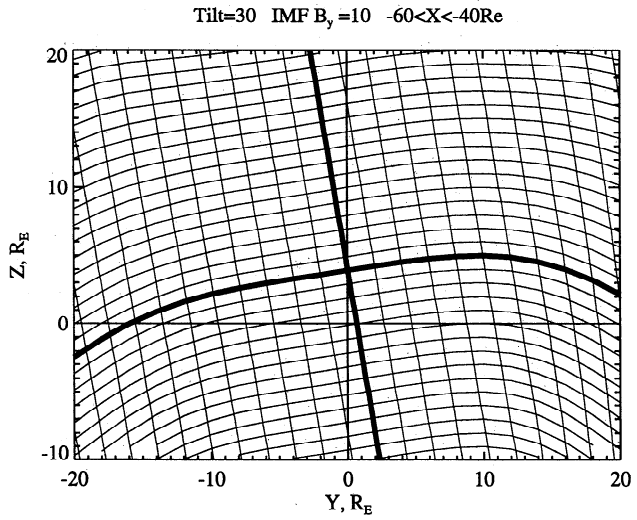

Figure 5. Illustration of the curvilinear coordinate system used in the local modeling of the tail field. Lines of the coordinates η and ζ are plotted for a specific set of warping/twisting parameters, obtained for the middle-tail bin $-60 < X < -40\ R_E$. Thick solid lines are for $\eta = 0$ and $\zeta = 0$.

One possible option is to define the coordinate η for any point (Y, Z) as the distance between that point and the one with the same value of ζ, but corresponding to the midnight meridian plane. Figure 5 displays the families of coordinate lines η and ζ for a specific set of the parameters R_H, G, L_y, T_1, and T_2, found from the Geotail data for the interval $-60 < X < -40$ and discussed in detail in the next section. Thick solid lines show the coordinate lines $\eta = 0$ and $\zeta = 0$.

The next step is to define a model for the distribution of the B_x in the two-dimensional space $\{\eta, \zeta\}$. Similarly to the Harris' model, we chose a simple form of the B_x variation across the current sheet:

$$B_x = B_0 \tanh\frac{\zeta}{D} \tag{4}$$

where both the asymptotic field B_0 and the scale half-thickness of the sheet D are functions of the distance η from the midnight meridian plane. In addition, B_0 is assumed to depend on the solar wind ram pressure P_d; however, we did not include here any dependence on the IMF, since it is of secondary importance in comparison with the pressure [*Tsyganenko*, 1996], and in this study we focus on the geometry of the current sheet, rather than on the lobe magnetic field. More specifically, we assumed

$$B_0 = B_{00} + B_{01}\left(\frac{\eta}{L_y}\right)^2 + B_{02}\sqrt{\frac{P_d}{\langle P_d\rangle}} \tag{5}$$

$$D = D_0 + D_1\left(\frac{\eta}{L_y}\right)^2 \tag{6}$$

Therefore besides the five parameters introduced when defining the warping and twisting geometry in (2)–(3), we have additional five parameters, entering in the model via the representation (4)–(6) for B_x. Of the 10 parameters, three are linear coefficients B_{00}, B_{01}, and B_{02}, while the remaining seven parameters, R_H, G, L_y, T_1, T_2, D_0, and D_1, are nonlinear.

The model parameters were sought by using a code, combining a standard least square fitting of the linear parameters and a Newton-LeCam-Marquardt algorithm for the search of nonlinear parameters and evaluation of the statistical errors, related to incomplete coverage by the data in individual bins. A detailed description of the method was published elsewhere [*Tsyganenko*, 1990] and hence will not be discussed in this paper. The results of the fitting are presented in the next section.

4. Warping and Twisting of the Current Sheet as Deduced From the Data

Table 1 contains the results of fitting the model given by (2)–(5) to the subsets of Geotail magnetometer data, corresponding to seven bins of X_{GSWM} and shown in Figures 1–3. The first three lines of the table provide the number of data points in each subset, the rms value of the B_x component, and the average value of the geodipole tilt angle. The number of data points in the first four bins is quite large, but it rapidly

Table 1. Parameters of Geotail Data Sets and of the Model Tail Current for Consecutive Bins of X

	$-15<X<-10$	$-20<X<-15$	$-25<X<-20$	$-30<X<-25$	$-40<X<-30$	$-60<X<-40$	$-100<X<-60$
				Data Set			
N	12833	12827	14694	14342	4264	7120	3054
$\langle B_x^2\rangle^{1/2}$	21.72	16.02	13.18	14.88	11.43	10.06	9.36
$\langle\Psi\rangle$	0.47	−9.97	−15.85	−19.40	−19.38	−16.60	−7.53
				Model			
B_{00}	17.0±0.50	11.4±0.53	11.1±0.54	13.2±0.77	6.08±1.1	1.71±0.40	3.76±0.67
B_{01}	−22.5±0.42	−12.7±0.44	−11.6±0.48	−12.1±1.0	−8.03 ±0.90	−7.46±0.49	−4.60±0.85
B_{02}	19.0±0.49	15.4±0.49	12.6±0.50	8.40±0.64	11.0±0.72	11.1±0.42	7.04±0.52
R_H	7.77±0.04	8.81±0.05	8.18±0.05	8.13±0.05	8.76±0.09	7.81±0.11	10.45±0.36
G	51.2±0.86	42.3±0.72	39.4±0.56	41.1±1.1	35.7±1.8	33.3±2.0	17.8±3.7
L_y^*	19.75	21.33	22.65	23.74	25.04	26.55	26.88
T_1	3.02±0.23	2.71±0.29	3.81±0.28	1.58±0.35	4.41±0.62	6.68±0.44	14.34±1.9
T_2	−2.45±0.46	−0.17±0.49	0.86±0.43	4.67±0.63	1.21±0.90	−2.04±0.67	−7.99±2.4
D_0	1.28±0.02	1.63±0.05	2.29±0.06	2.82±0.10	3.05±0.20	2.39±0.11	6.08±0.44
D_1^*	4.0	4.0	4.0	4.0	4.0	4.0	4.0
σ	8.36	8.06	6.85	7.04	7.21	6.23	5.76
$\langle B_x^2\rangle^{1/2}/\sigma$	2.60	1.99	1.92	2.11	1.59	1.61	1.62

*Fixed parameter

drops down tailward from $X = -30$, which results in generally larger errors. However, as will be shown below, even for the farthest bin, the obtained characteristics of the current sheet are still quite reasonable. As would be expected, the rms value of the measured B_x component decreases down the tail almost monotonically; an anomalous increase is observed in the bin $-30 < X - 25\,R_E$ and is probably due to a larger relative number of lobe measurements in that bin. As was already noted above, the average geodipole tilt angles for most of the bins are negative, reaching $-19.4°$ for the bin $-30 < X - 25\,R_E$; fortunately, this bias significantly improves the coverage of the current sheet, owing to the tilt-related shift of the sheet southward from the equatorial plane, where most of the data points are located (Figures 2 and 3, bottom left panels).

Before concentrating on individual model parameters, we briefly comment on the overall indicators of the goodness of the fit. These indicators are the rms residual field, $\sigma = \langle(B_{x\,mod} - B_{x\,meas})^2\rangle^{1/2}$, and the figure of merit $\langle B_x^2\rangle^{1/2}/\sigma$ given in the two last lines of Table 1. The general trend is toward lower values of σ for larger tailward distances. However, owing to an even faster decrease of the measured rms field, the figure of merit is also falling off, from 2.6 for the closest bin to 1.6 for the farthest one, reflecting both larger variability of the distant field and steadily increasing inaccuracy of the correction for the windsock effect, as one proceeds further down the tail. In this regard, it is interesting to estimate the effect of replacing the GSM coordinates by the GSWM coordinates, based on the observed direction of the solar wind. To this end, we ran once again the same fitting code for the same data subsets; however, this time the coordinates η and ζ in (3)–(6) were calculated from standard (GSM) coordinates of the data points, rather than from corrected (GSWM) ones. It was found that the correction procedure improved the figure of merit in the middle tail, between $X = -20$ and $X = -60\,R_E$, with best results obtained for the bins $-60 < X < -40$ and $-30 < X < -25$ (~10% and ~12% increase, respectively). Surprisingly, the opposite result was obtained for the two nearest bins, where switching to the GSWM coordinates decreased the figure of merit by 5–10%, instead of having improved the fit. A probable reason for that decrease can be a significantly slower response of the near-Earth magnetotail to changes in the solar wind direction, as compared with the distant tail.

The values of the model parameters in Table 1 are provided with estimates of their errors, calculated under the assumption that both the random component in the measured values of B_x and the parameters themselves have a normal distribution around their most probable values and that there is no residual systematic error in the model description of the tail magnetic field. Both assumptions are questionable and hard to verify; for that reason the values of the errors given in the table should be considered as a rough order-of-magnitude estimate. Nonetheless, they can be quite helpful in defining the degree of the model's flexibility. In particular, in the initial test runs we allowed L_y to be varied along with the rest of the model parameters. However, it was found that in most cases L_y showed a high (97–99%) correlation with G, accompanied with an increased error in either of the the two parameters and irregular changes from one X bin to another. For that reason it was decided to consider L_y as a fixed parameter in the least squares search. More specifically, for each X bin, L_y was set equal to the corresponding dawn-dusk radius of the average model magnetopause, used in the selection of the data (section 2.2.1). The same decision was made with regard to the parameter D_1, which controls the rate of thickening of

the current sheet toward the flanks. No reasonable trend was found in its behavior, and hence it was fixed equal to 4 R_E, on the order of its average estimate from the initial trial runs.

Inspection of the first three linear parameters in Table 1 shows several notable features. First, the average total lobe field at the midnight meridian, given by the sum $B_{00} + B_{02}\sqrt{P_d/\langle P_d\rangle}$, monotonically decreases tailward, so that, assuming $P_d = \langle P_d\rangle$ and $\eta = 0$, one obtains from (5) $B_x \approx 36$nT for the nearest X bin and $B_x \approx 10.8$nT for the farthest one. Both estimates agree quite well with previous results: the near-tail lobe field strength is within the range of values obtained by *Fairfield and Jones* [1996] (see their Figure 4), while the magnitude of the far tail field is close to the result of *Yamamoto et al.* [1994] (presented in their Figure 3).

Second, in all the bins the coefficient B_{01}, controlling the rate of the field variation parallel to the current sheet in the dawn-dusk direction, is negative and comparable with B_{00} and B_{02}. Assuming $P_d = \langle P_d\rangle$ and $\eta = L_y$ in (5), we find that the tail lobe field magnitude drops by 40–60% between the midnight meridian and the tail's flanks for the entire range of X from -10 to -100 R_E.

Third, the coefficients B_{00} and B_{02} have comparable values in the near tail, while for the last three bins B_{02} becomes predominant, owing to a somewhat slower rate of its tailward decrease. This fact means that the lobe field in the far tail is more sensitive to solar wind pressure, as compared with the near tail: using the coefficients obtained, we find from (4) and (5) that an increase in P_d from 3 nPa to 6 nPa results in a ≈22% increase of B_x in the $-15 < X < -10$ bin, compared with ≈36% and ≈27% for $-60 < X < -40$ and $-100 < X < -60$, respectively.

Inspection of the obtained nonlinear parameters also reveals interesting facts. The hinging distance R_H does not show any orderly dependence on the tailward distance and remains within the range $7.8 \le R_H \le 10.4$ in the entire interval of X. There is no indication that the amplitude of the tilt-related north-south motion of the tail current sheet falls off to zero in the distant tail.

The warping amplitude G is maximal in the closest bin and significantly decreases tailward, so that in the farthest bin the current sheet is much closer to a planar surface. As would be expected, the accuracy of determination of both tilt-related parameters (as is the case for all other parameters) is best for the closest bin and decreases tailward.

The thickness of the current sheet D_0 almost monotonically increases tailward. However, we cannot unambiguously determine to what extent this effect is due to actual thickening of the sheet and how large the contribution is from chaotic flapping motions, passage of plasmoids, and errors in the determination of the tail axis orientation.

Now let us turn to the effects of the IMF B_y. First of all, note that the relative errors in the estimated values of the IMF-related coefficients T_1 and T_2 are significantly larger than those for the tilt-related terms. In part, this is due to inevitable errors in the procedure of extrapolating to the location of Geotail of the IMF components, observed by Wind at relatively large sunward distances, as well as due to inaccuracies of the transformation from GSE to GSWM coordinates. In addition, the tail's response to IMF conditions is not as straightforward as that due to the dipole tilt; a more detailed study may be necessary, which would take into account a finite time of the IMF-related magnetic flux transfer.

In spite of all these caveats, our study revealed quite reasonable behavior of the current sheet in response to the IMF B_y component. The coefficient T_1, defining the amplitude of the rotation of the sheet around the X axis per 1 nT of B_y has a clear tendency to increase tailward, from $T_1 \sim 3$ in the closest bin to $T_1 \sim 14$ in the farthest one. The second IMF-related parameter, T_2, is negative at the ends of the studied interval of X but rises to positive value $T_2 \approx 4.7$ in the midtail, which results in an S-like shape of the sheet cross section, found earlier by *Kaymaz et al.* [1995b] for the same range of the X coordinate using IMP 8 data. In comparison with other parameters, T_2 has the largest relative error, and although it shows quite regular variation with X, it still remains unclear whether the obtained values reflect any real effect.

The above discussed features can be visualized by plotting the profiles of the current sheet surface given by the model (2) with coefficients from Table 1, for all seven bins of X. Figure 6 displays the shapes of the current sheet in the same order with regard to X binning as the corresponding data are shown in Figures 1–3. All the plots correspond to the same values of the geodipole tilt, $\Psi = 30°$, and of the IMF $B_y = 10$ nT. The solid line shows the resultant shape of the sheet, including both tilt- and IMF-induced warping, while the dashed and dotted lines represent separate contributions from these two effects, respectively.

There is an interesting implication of our finding that the warping weakens with X away from Earth, while the hinging distance does not decrease. As can be seen in the bottom right panel of Figure 6, it should result in an imbalance of the magnetic flux between the northern and southern lobes, unless we assume that the tail boundary shifts in the same direction as the current sheet, in response to the geodipole tilt. This conjecture is supported by initial results of an inspection of the data of magnetopause crossings; a more detailed discussion of this effect extends beyond the frame of this paper and is relegated to a separate study.

Table 2 and Figure 7 display in similar format the results obtained by using ISEE 1/2 data. Compared with the corresponding Geotail results in the first two panels of Figure 6, the plots in Figure 7 reveal much similarity both in the tilt effects and in the IMF-induced twisting. The most conspicuous difference between the Geotail and ISEE results can be seen in the shape of the dotted curve in the second panel; while the Geotail data predict almost pure rotation of the current sheet in response to IMF B_y, without the S-shaped warping, the ISEE data yield a distinct S-like deformation, but no visible rotation of the sheet. The most probable cause of the difference between ISEE and Geotail results is a significant difference in the spatial distribution of the data, evident from the comparison of the corresponding panels of Figures 3 and 4. The combined gross effect, however, is the same in both cases: the current sheet responds to IMF B_y in the expected way, the overall deformation magnitudes are quite similar, and the twisting is discernible quite close to Earth.

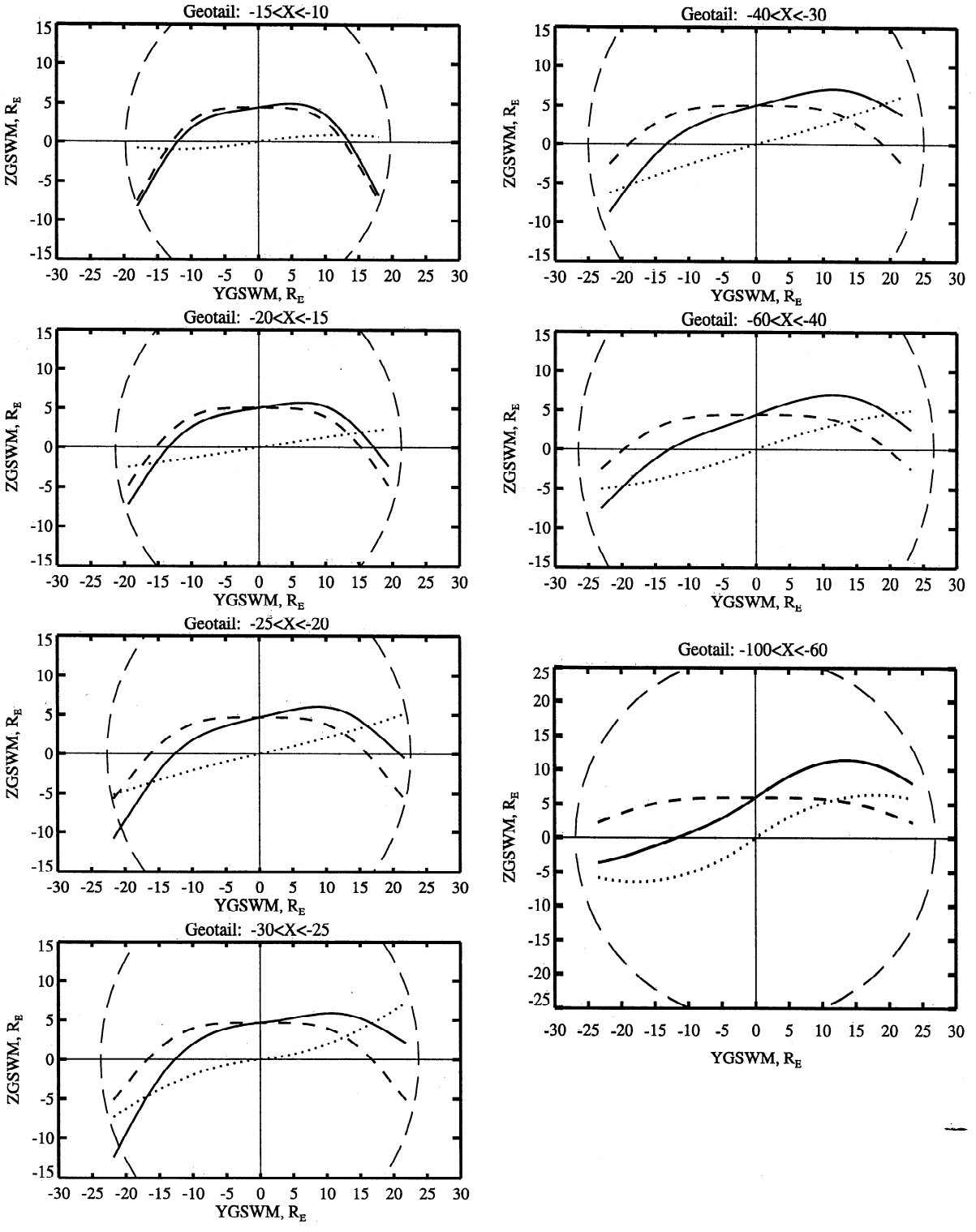

Figure 6. Shapes of the model current sheet in the tail cross sections, obtained from the binned Geotail data sets of Figure 3. All the plots correspond to the same values of the Earth's dipole tilt, $\Psi = 30°$, and of the IMF B_y = 10 nT. Dashed and dotted lines show separate contributions of the tilt-related warping/hinging and of the IMF-related twisting, respectively. Note a steady increase in the twisting angle, from the nearest to farthest bin of X.

Table 2. Same as Table 1, Derived From ISEE 1/2 data

	$-15<X<-10$	$-20<X<-15$
	Data Set	
N	8995	8340
$\langle B_x^2\rangle^{1/2}$	27.54	24.26
	Model	
B_{00}	22.5±0.4	14.1±0.3
B_{01}	−25.7±0.4	−17.6±0.7
B_{02}	18.5±0.4	16.7±0.3
R_H	8.01±0.07	8.12±0.07
G	45.2±0.7	36.3±1.3
L_y^*	19.75	21.33
T_1	0.11±0.17	−1.18±0.34
T_2	0.795±0.31	6.77±0.69
D_0	1.72±0.04	2.05±0.04
D_1^*	4.0	4.0
σ	8.51	6.84

*Fixed parameter

5. Conclusions and Remarks on the Inclusion of the Twisting Effect in Magnetic Field Models

The purpose of this work was to quantitatively estimate the amplitude of the tilt- and IMF-related deformation of the cross-tail current at different tailward distances. The results of this study are intended to be used in the construction of global data-based models of the magnetosphere, extending the spatial range of their validity to larger tailward distances.

We have found that the tilt-related oscillation of the current sheet in the north-south direction persists up to ~100 R_E down the tail, and there is no indication of any decrease of its amplitude with growing geocentric distance. The hinging distance lies in the range between 7.4 and 10.4 R_E, in agreement with previous results, obtained for the near- and middle-tail regions. In contrast, the current sheet warping in the Y-Z plane is the strongest at close distances from Earth but gradually fades away down the tail.

Modeling of the IMF-related twisting of the tail current sheet, based on Geotail and ISEE data, revealed a well-pronounced effect even as close to Earth as R ~10-15 R_E. As would be expected from a theoretical viewpoint, the twisting angle steadily grows with geocentric distance, so that at lunar distances it can reach quite significant values of 20°–30° for IMF $B_y = 10$ nT.

On the basis of the assumed functional form (2) for the local description of the hinging/warping/twisting effect, we can find suitable approximations for the X dependence of the parameters R_H, G, L_y, T_1, and T_2 and thus devise a global representation of the geometry of the magnetotail current sheet. However, that would solve only a part of the entire problem: the remaining big question is how to extend the existing mathematical model of the tail magnetic field, in order to incorporate the new geometrical effects. *Tsyganenko* [1995] suggested a method for the inclusion of the hinging/warping effect in the global field model, based on modifying initial vector potentials for the field of the cross-tail current and adopting an extended expansion for the shielding field, which included tilt-dependent terms and ensured full confinement of the total tail field within a prescribed magnetopause.

The same approach can in principle be pursued for the inclusion of the twisting effect, taking advantage of the relatively slow variation of the twisting angle along the Sun-Earth line. Although that method is likely to lead one to the desired result, it would also require a further increase in the number of terms in the shielding field expansions, making the computation algorithm even more cumbersome and slow. *Kullen and Blomberg* [1996] suggested a simple modification of the data-based model of *Tsyganenko* [1989], in order to simulate the twisting effect due to the IMF B_y. They added a divergence-free term to the original untilted T89 field, which resulted in a desirable twisting of the surface $B_x = 0$.

An attractive alternative for incorporating the twisting effect is suggested below, based on a simple transformation of the existing model magnetic field. Namely, suppose

$$\vec{\mathbf{B}} = \vec{\mathbf{e}}_\rho B_\rho + \vec{\mathbf{e}}_\phi B_\phi + \vec{\mathbf{e}}_x B_x \tag{7}$$

is the untwisted magnetic field of the tail current system, including the field of the shielding currents on the magnetopause, written in the cylindrical coordinate system $\{\rho, \phi, X\}$ in which the X axis coincides with the Sun-Earth line. Replace the variable ϕ by $\phi^* = \phi - \phi_0(X)$, where ϕ_0 is the twist-

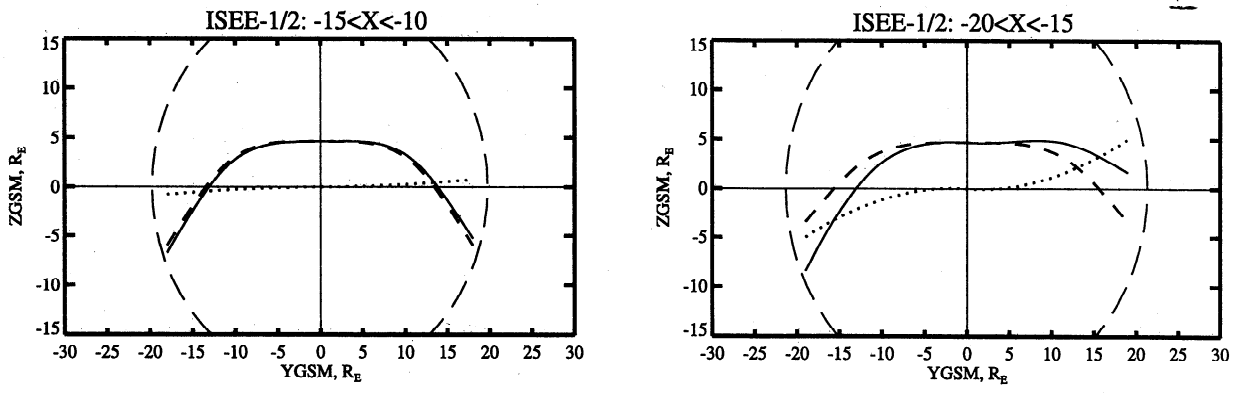

Figure 7. Same as in Figure 6, but for the two nearest bins, obtained from ISEE 1/2 data. Compare with plots in the two upper left panels of Figure 6.

ing angle, equal to zero near Earth and gradually increasing in the antisunward direction. One can see that the modification results in an additional term $-\left(\partial B_x^*/\partial\phi^*\right)\left(\partial\phi_0/\partial X\right)$ in the expression for the divergence of the magnetic field, which violates the condition $\nabla\cdot\vec{\mathbf{B}}=0$. It can be easily verified that, in order to restore that condition, it suffices to add an additional term to B_ϕ^*, equal to $\rho B_\phi^*\partial\phi_0/\partial X$. The meaning of the additional term is quite simple: $\rho\partial\phi_0/\partial X$ is the tangent of the angle between the incremental shift along the X axis and the azimuthal shift due to the twisting, which is just the geometrical factor, providing the correct ratio between B_x and B_ϕ.

The above procedure can be further generalized by adding a radial dependence of the twisting angle, so that now $\phi_0=\phi_0(\rho, X)$. In this case we have to add a second correction term to B_ϕ^*, equal to $\rho B_\rho^*\partial\phi_0/\partial\rho$. After some algebra, we obtain the final expressions for the two-dimensional "twist transformation" in the form

$$\begin{aligned} B_x &= B_x^* \\ B_y &= B_y^*\cos\phi_0 - B_z^*\sin\phi_0 - Z\left(B_\rho^*\frac{\partial\phi_0}{\partial\rho}+B_x^*\frac{\partial\phi_0}{\partial X}\right) \\ B_z &= B_y^*\sin\phi_0 + B_z^*\cos\phi_0 + Y\left(B_\rho^*\frac{\partial\phi_0}{\partial\rho}+B_x^*\frac{\partial\phi_0}{\partial X}\right) \end{aligned} \tag{8}$$

where the asterisks indicate that the original azimuthal coordinate ϕ has been replaced by the modified one, $\phi^*=\phi-\phi_0(\rho, X)$.

Figure 8 displays the result of applying the twist transformation to the magnetic field given by the model of *Tsyganenko* [1996]. The twisting function $\phi_0(\rho, X)$ in this example was not based on any data; rather, we chose a simple analytical expression, in order to numerically check the method and visualize the twisted distribution of the spread-out electric current. The figure displays the isointensity contours of the total volume current density in the cross section of the model magnetotail at $X=-70\,R_E$, subject to the strong twisting. As one can see in the plot, the current remains concentrated within a thin sheet, deformed into an S-shaped band, as specified by the adopted twisting function.

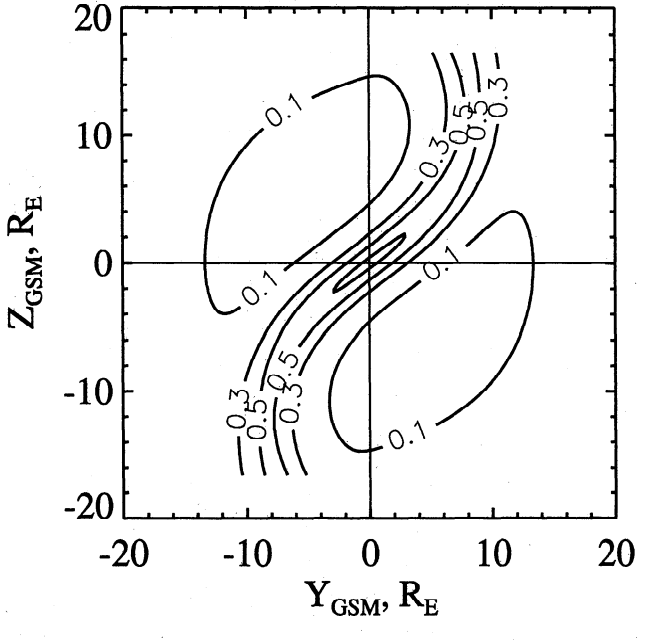

Figure 8. Illustration of the twist transformation. The plot displays a family of lines of equal volume current density in a strongly twisted field of the model magnetotail, obtained by applying the transformation to the magnetosphere model by *Tsyganenko* [1996].

The proposed twist transformation is mathematically simple, allows for an arbitrary variation of the twist angle $\phi_0(X)$ along the tail axis, and can be used with any model field. It is also important that, since the twisting is applied to the total magnetospheric $\vec{\mathbf{B}}$ vector, it does not violate the condition of full shielding of the tail magnetic field inside the magnetopause.

Appendix: Geocentric Solar Wind Magnetospheric Coordinates

The GSWM coordinate system has its X axis pointing from Earth antiparallel to the solar wind flow vector $\vec{\mathbf{V}}$, so that the first orthonormal vector

$$\vec{\mathbf{e}}_\alpha = -\vec{\mathbf{V}}/V \tag{A1}$$

The second unit vector, $\vec{\mathbf{e}}_\beta$, can be found by normalizing the vector product $\vec{\mu}\times\vec{\mathbf{e}}_\alpha$, where $\vec{\mu}=-\vec{\mathbf{M}}_E/M_E$ is the unit vector antiparallel to Earth's dipole moment $\vec{\mathbf{M}}_E$. Hence

$$\vec{\mathbf{e}}_\beta = \frac{\vec{\mu}\times\vec{\mathbf{e}}_\alpha}{\left|\vec{\mu}\times\vec{\mathbf{e}}_\alpha\right|}\,. \tag{A2}$$

The third unit vector, as usual, completes the right-handed orthonormal basis:

$$\vec{\mathbf{e}}_\gamma = \vec{\mathbf{e}}_\alpha\times\vec{\mathbf{e}}_\beta \tag{A3}$$

The above transformations can be conveniently specified step by step, on the basis of the standard GSM coordinates as follows:

1. In the original high-resolution data base, the solar wind velocity vectors had already been corrected for the aberration due to Earth's orbital motion, that is, the V_y component in the geocentric solar ecliptic coordinate system was reduced by 29 km/s. Therefore, the first step is to transform the vector $\vec{\mathbf{V}}$ back to the standard GSE coordinates by adding 29 km/s to V_y.

2. Based on the current year, date, and UT, transform $\vec{\mathbf{V}}$ to GSM coordinates and find GSM components of $\vec{\mathbf{e}}_\alpha$ from (A1). The transformation can be done by using the software GEOPACK, available from our website: http://www-spof.gsfc.nasa.gov/Modeling/geopack.html.

3. In the GSM coordinates the vector $\vec{\mu}$ has components $\{\sin\Psi, 0, \cos\Psi\}$, where Ψ is the geodipole tilt angle. Hence the vector $\vec{\mathbf{P}}=\vec{\mu}\times\vec{\mathbf{e}}_\alpha$ in (A2) has components

$$\begin{aligned} P_x &= -\vec{\mathbf{e}}_{\alpha y}\cos\Psi \\ P_y &= \vec{\mathbf{e}}_{\alpha x}\cos\Psi - \vec{\mathbf{e}}_{\alpha z}\sin\Psi \\ P_z &= \vec{\mathbf{e}}_{\alpha y}\sin\Psi \end{aligned} \tag{A4}$$

which allows one to find $\vec{\mathbf{e}}_\beta = \vec{\mathbf{P}}/P$ and, using (A3), find $\vec{\mathbf{e}}_\gamma$.

4. Based on the above defined orthonormal basis $\{\vec{\mathbf{e}}_\alpha, \vec{\mathbf{e}}_\beta, \vec{\mathbf{e}}_\gamma\}$ any vector $\vec{\mathbf{A}}$ can be transformed from GSM to GSWM coordinates by $\vec{\mathbf{A}}^{GSWM} = \hat{\mathbf{T}}\,\vec{\mathbf{A}}^{GSM}$, where the rows of the matrix $\hat{\mathbf{T}}$ for the transformation from GSM to GSWM coordinates are composed of the components of the vectors $\vec{\mathbf{e}}_\alpha$, $\vec{\mathbf{e}}_\beta$, and $\vec{\mathbf{e}}_\gamma$, respectively.

Acknowledgments. The data of ISEE 1/2 spacecraft were provided by National Space Science Data Center, GSFC. This work is supported by NASA grants NAS5-32350, NASW-97024 (ISTP GI Program) and NSF Magnetospheric Physics Program grant ATM-9501463.

The Editor thanks Tuija Pulkkinen and George Siscoe for their assistance in evaluating this paper.

References

Bowling, S. B., The influence of the direction of the geomagnetic dipole on the position of the neutral sheet, *J. Geophys. Res., 79,* 5155, 1974.

Bowling, S. B., and C. T. Russell, The position and shape of the neutral sheet at 30-R_E distance, *J. Geophys. Res., 81,* 270, 1976.

Collier, M. R., J. A. Slavin, R. P. Lepping, K. Ogilvie, A. Szabo, H. Laakso, and S. Taguchi, Multispacecraft observations of sudden impulses in the magnetotail caused by solar wind pressure discontinuities, *J. Geophys. Res.,* in press, 1998.

Cowley, S. W. H., Magnetospheric asymmetries associated with the Y-component of the IMF, *Planet. Space Sci., 29,* 79, 1981.

Crooker, N. U., G. L. Siscoe, C. T. Russell, and E. J. Smith, Factors controlling degree of correlation between ISEE 1 and ISEE 3 interplanetary magnetic field measurements, *J. Geophys. Res., 87,* 2224, 1982.

Dandouras, J., On the average shape and position of the geomagnetic neutral sheet and its influence on plasma sheet statistical studies, *J. Geophys. Res., 93,* 7345, 1988.

Fairfield, D. H., A statistical determination of the shape and position of the geomagnetic neutral sheet, *J. Geophys. Res., 85,* 775, 1980.

Fairfield, D. H., and J. Jones, Variability of the tail lobe field strength, *J. Geophys. Res., 101,* 7785, 1996.

Gosling, J. T., D. J. McComas, M. F. Thomsen, S. J. Bame, and C. T. Russell, The warped neutral sheet and plasma sheet in the near-Earth geomagnetic tail, *J. Geophys. Res., 91,* 7093, 1986.

Harris, E. G., On a plasma sheath separating regions of oppositely directed magnetic field, *Nuovo Cimento Soc. Ital. Fis., 23,* 116, 1962.

Hilmer, R. V., and G.-H. Voigt, A magnetospheric magnetic field model with flexible current systems driven by independent physical parameters, *J. Geophys. Res., 100,*, 5613, 1995.

Kaymaz, Z., H. E. Petschek, G. L. Siscoe, L. A. Frank, K. L. Ackerson, and W. R. Paterson, Disturbance propagation times to the far tail, *J. Geophys. Res., 100,* 23743, 1995a.

Kaymaz, Z., G. L. Siscoe, J. G. Luhmann, J. A. Fedder, J. G. Lyon, Interplanetary magnetic field control of magnetotail field: IMP 8 data and MHD model compared, *J. Geophys. Res., 100,* 17163, 1995b.

King, J. H., Availability of IMP 7 and IMP 8 data for the IMS period, in: *The IMS Source Book,* edited by C. T. Russell and D. J. Southwood, 304 pp., AGU, Washington, D. C., 1982.

Kokubun, S., T. Yamamoto, M. H. Acuna, K. Hayashi, K. Shiokawa, and H. Kawano, The Geotail magnetic field experiment, *J. Geomagn. Geoelectr., 46,* 7, 1994.

Kullen, A., and L. G. Blomberg, The influence of IMF B_y on the mapping between the Earth's magnetotail and its ionosphere, *Geophys. Res. Lett., 23,* 2561, 1996.

Lepping, R. P., et al., The WIND magnetic field investigation, *Space Sci. Rev., 71,* 207, 1995.

McComas, D. J., C. T. Russell, R. C. Elphic, and S. J. Bame, The near-Earth cross-tail current sheet: Detailed ISEE 1 and 2 case studies, *J. Geophys. Res., 91,* 4287, 1986.

Nakai, H., Y. Kamide, and C. T. Russell, Statistical nature of the magnetotail current in the near-Earth region, *J. Geophys. Res., 102,* 9573, 1997.

Nishida, A., The GEOTAIL mission, *Geophys. Res. Lett., 21,* 2871, 1994.

Ogilvie, K. W., et al., SWE, A comprehensive plasma instrument for the WIND spaceceraft, *Space Sci. Rev., 71,* 55, 1995.

Owen, C. J., J. A. Slavin, I. G. Richardson, N. Murphy, and R. J. Hynds, Average motion, structure and orientation of the distant magnetotail determined from remote sensing of the edge of the plasma sheet boundary layer with $E > 35$ keV ions, *J. Geophys. Res., 100,* 185, 1995.

Peredo, M., J. A. Slavin, E. Mazur, and S. A. Curtis, Three-dimensional position and shape of the bow shock and their variation with Alfvenic, sonic, and magnetosonic Mach numbers and interplanetary magnetic field orientation, *J. Geophys. Res., 100,* 7907, 1995.

Russell, C. T., The configuration of the magnetosphere, in *Critical Problems of Magnetospheric Physics,* edited by E. R. Dyer, pp.1–16, IUCSTP Secretariat, National Academy of Sciences, Washington, D. C., 1972.

Russell, C. T., ISEE 1 and 2 fluxgate magnetometers, *IEEE Trans. Geosci. Electron., GE-16,* 239, 1978.

Russell, C. T, and K. I. Brody, Some remarks on the position and shape of the neutral sheet, *J. Geophys. Res., 72,* 6104, 1967.

Sergeev, V. A., N. P. Dmitrieva, and E. S. Barkova, Triggering of substorm expansion by the IMF discontinuities: Time delay analysis, *Planet. Space Sci., 34,* 1109, 1986.

Sibeck, D. G., G. L. Siscoe, J. A. Slavin, E. J. Smith, B. T. Tsurutani, and R. P. Lepping, The distant magnetotail's response to a strong interplanetary magnetic field B_y: Twisting, flattening, and field line bending, *J. Geophys. Res., 90,* 4011, 1985.

Sibeck, D. G., J. A. Slavin, E. J. Smith, and B. T. Tsurutani, Twisting of the geomagnetic tail, in *Solar Wind–Magnetosphere Coupling,* edited by Y. Kamide and J. A. Slavin, p. 731, Terra Sci., Tokyo, 1986.

Sibeck, D. G., R. E. Lopez, and E. C. Roelof, Solar wind control of the magnetopause shape, location, and motion, *J. Geophys. Res., 96,* 5489, 1991.

Slavin, J. A., E. J. Smith, D. G. Sibeck, D. N. Baker, R. D. Zwickl, and S.-I. Akasofu, An ISEE 3 study of average and substorm conditions in the distant magnetotail, *J. Geophys. Res., 90,* 10,875, 1985.

Slavin, J. A., M. R. Collier, R. P. Lepping, and A. Szabo, Characteristics of IMF correlations determined with the WIND and IMP 8 spacecraft, *Eos Trans. AGU, 78*(17), Spring Meet. Suppl., S264, 1997.

Tsyganenko, N. A., A magnetospheric magnetic field model with a warped tail current sheet, *Planet. Space Sci., 37,* 5, 1989.

Tsyganenko, N. A., Quantitative models of the magnetospheric magnetic field: methods and results, *Space Sci. Rev., 54,* 75, 1990.

Tsyganenko, N. A., Modeling the Earth's magnetospheric magnetic field confined within a realistic magnetopause, *J. Geophys. Res., 100,* 5599, 1995.

Tsyganenko, N. A., Effects of the solar wind conditions on the global magnetospheric configuration as deduced from data-based field models, in *Eur. Space Agency Spec. Publication ESA SP-389,* 181, 1996.

Voigt, G.-H., A mathematical magnetospheric field model with independent physical parameters, *Planet. Space Sci., 29,* 1, 1981.

Yamamoto, T., K. Shiokawa, and S. Kokubun, Magnetic field structures of the magnetotail as observed by GEOTAIL, *Geophys. Res. Lett., 21,* 2875, 1994.

S. B. P. Karlsson, Swedish Institute of Space Physics, S-755 91 Uppsala, Sweden. (e-mail: peter@milak.irfu.se)

S. Kokubun, Solar-Terrestrial Environment Laboratory, Nagoya University, Honohara, Toyokawa 442, Japan. (e-mail: kokubun@stelab.nagoya-u.ac.jp)

A. J. Lazarus, Center for Space Research, Massachusetts Institute of Technology, Cambridge, MA 02139. (e-mail: ajl@spacc.mit.edu)

K. W. Ogilvie and J. A. Slavin, Laboratory for Extraterrestrial Physics, NASA Goddard Space Flight Center, Greenbelt, MD 20771. (e-mail: u2kwo@lepvax.gsfc.nasa.gov, slavin@lepjas.gsfc.nasa.gov)

C. T. Russell, Institute of Geophysics and Planetary Physics, University of California, Los Angeles, 6877 Slichter Hall, Los Angeles, CA 90095-1567. (e-mail: ctrussel@igpp.ucla.edu)

N. A. Tsyganenko, Hughes STX Corporation, Laboratory for Extraterrestrial Physics, Code 695, NASA Goddard Space Flight Center, Greenbelt, MD 20771. (e-mail: kolya@nssdca.gsfc.nasa.gov)

T. Yamamoto, Institute of Space and Astronautical Science, 3-1-1 Yoshinodai, Sagamihara 229, Japan. (e-mail: yamamoto@gtl.isas.ac.jp)

(Received October 9, 1997; revised November 19, 1997; accepted November 24, 1997.)